Accurate *ab initio* tight-binding Hamiltonians: Effective tools for electronic transport and optical spectroscopy from first principles

Pino D'Amico,[1,2] Luis Agapito,[3,4] Alessandra Catellani,[2] Alice Ruini,[1,2] Stefano Curtarolo,[3,5] Marco Fornari,[3,6] Marco Buongiorno Nardelli,[3,7,*] and Arrigo Calzolari[2,3,4,†]

[1]*Dipartimento di Fisica, Informatica e Matematica, Universitá di Modena and Reggio Emilia, Via Campi 213/a, 41125 Modena, Italy*

[2]*CNR-NANO Research Center S3, Via Campi 213/a, 41125 Modena, Italy*

[3]*Center for Materials Genomics, Duke University, Durham, North Carolina 27708, USA*

[4]*Department of Physics, University of North Texas, Denton, Texas 76203, USA*

[5]*Materials Science, Electrical Engineering, Physics and Chemistry, Duke University, Durham, North Carolina 27708, USA*

[6]*Department of Physics, Central Michigan University and Science of Advanced Materials Program, Mt. Pleasant, Michigan 48859, USA*

[7]*Department of Physics and Department of Chemistry, University of North Texas, Denton, Texas 76203, USA*

(Received 19 August 2016; published 26 October 2016)

The calculations of electronic transport coefficients and optical properties require a very dense interpolation of the electronic band structure in reciprocal space that is computationally expensive and may have issues with band crossing and degeneracies. Capitalizing on a recently developed pseudoatomic orbital projection technique, we exploit the exact tight-binding representation of the first-principles electronic structure for the purposes of (i) providing an efficient strategy to explore the full band structure $E_n(\mathbf{k})$, (ii) computing the momentum operator differentiating directly the Hamiltonian, and (iii) calculating the imaginary part of the dielectric function. This enables us to determine the Boltzmann transport coefficients and the optical properties within the independent particle approximation. In addition, the local nature of the tight-binding representation facilitates the calculation of the ballistic transport within the Landauer theory for systems with hundreds of atoms. In order to validate our approach we study the multivalley band structure of $CoSb_3$ and a large core-shell nanowire using the ACBN0 functional. In $CoSb_3$ we point the many band minima contributing to the electronic transport that enhance the thermoelectric properties; for the core-shell nanowire we identify possible mechanisms for photo-current generation and justify the presence of protected transport channels in the wire.

DOI: 10.1103/PhysRevB.94.165166

I. INTRODUCTION

The ability to efficiently generate and manage a combination of theoretical and experimental data is the foundation for data-driven discovery of new materials and functions as well as methods to control manufacturing processes [1,2]. This formidable task requires a continuous feedback loop where descriptors [2] of the functional properties are calculated for an enormous number of materials configurations, integrated in the databases [3–6], compared with the available experiments, and exploited in the prediction cycle. In this paper we focus on a broad class of descriptors derived from the electronic structure calculations in order to provide easier integration with the experimental data. We introduce tight-binding methodologies for the calculation of electronic transport properties and the simulation of optical spectroscopies in the broadest energy range and with excellent accuracy as well as high computational efficiency.

The prerequisite for the simulation of both electron transport and optical properties is the accurate evaluation of the electronic structure of the system that is obtained by a fully self-consistent quantum-mechanical calculation either within density functional theory (DFT) or other first-principles approaches. The electronic structure of solids is often described with Fourier basis functions that account naturally for the periodicity and whose completeness is easily improvable up to any desirable accuracy. The delocalized character of plane waves, however, is not appropriate for the description of highly localized electronic systems unless a very large number of basis functions is used. The development of minimal-space solutions such as atomic orbital (AO) Bloch sums, which are capable of capturing with satisfactory accuracy the properties of solids and molecules on finite Hilbert spaces, has been central to methodological developments in quantum chemistry and solid-state physics for many decades.

Atomic orbital basis sets provide the foundation for methods, such as tight binding (TB), which combine an intuitive physical representation of the interactions, low computational cost, and interesting alternatives for the study of the electronic structure of molecules and solids [7–9]. The TB Hamiltonian matrix is the central quantity that provides a compact real space representation of the many-body interactions, the accuracy of the electronic structure relies on the quality of such matrix. Albeit computationally inexpensive and very intuitive for simple compounds, semiempirical TB implementations often fail in the prediction of electronic structure of complex materials and, in most cases, lack of predictive value when dealing with structural and chemical modifications as well as charge rearrangements. In recent years, the reliability of the TB models has been largely improved with the introduction of *ab initio* TB Hamiltonians derived from fully self-consistent quantum-mechanical calculations through a mapping into a much smaller space spanned by a set of atomic or atomiclike orbitals. This procedure combines the accuracy and the predictive value of first-principles approaches with the low computational cost of TB techniques. Furthermore, it is

*mbn@unt.edu

†arrigo.calzolari@nano.cnr.it

particularly useful for the evaluation of properties such as the electron conductivity and the optical absorption spectra that require a precise and ultrafine reciprocal space integration, typically very computationally expensive.

We recently developed a straightforward, noniterative projection scheme that can exactly represent the first-principles electronic structure of a periodic system on a finite AO-like basis [10–12]. By filtering the projections of Bloch states with high-kinetic-energy components and tuning the richness of the finite Hilbert space, we construct fully first-principles TB Hamiltonians where the number of exactly reproduced bands with respect to the original DFT calculation can be selectively increased at a negligible computational cost. This provides cost-effective solutions to design efficient algorithms for electronic structure simulations of realistic material systems and massive high-throughput investigations. Our technique does not seek construction of (heavily customized, localized) basis functions. Its value resides on allowing noniterative reproduction of a large number of energy bands using standard quantum-chemistry basis sets or the pseudoatomic orbitals (PAO) of a standard pseudopotential calculation. Practically, the present methodology completely supersedes the need for engineered basis functions such as maximally localized Wannier functions [13] or muffin-tin orbitals of arbitrary order (NMTO) [14] in the context of the evaluation of transport [15–17] or optical properties. Moreover, the knowledge of a localized orbital representation that maps seamlessly the electronic structure onto a localized AO basis set that is eventually fitted to a Gaussian basis set, opens the way to the fast (analytical) computation of two-electron integrals for solid-state applications and it is at the core of the development of the accurate and efficient ACBN0 functional [18].

The paper is organized as follows: in Sec. II we will discuss the theoretical background and the practical implementation of the procedure with representative test cases. In Sec. III we summarize the computational details of this study. In Sec. IV we study, with our methodology, two significant materials problems in order to show the importance of fine reciprocal space sampling and the computational efficiency of the PAO projection to deal with very large systems. We chose to study the thermoelectric properties of $CoSb_3$ and the transport and optical properties of core-shell nanowire of ZnO and ZnS. Finally, in Sec. V we outline the conclusions of the present work.

II. METHODOLOGY

A. TB representation from PAO projections

Accurate TB Hamiltonian matrices can be built from the direct projection of the Kohn-Sham (KS) Bloch states $|\psi_{n\mathbf{k}}\rangle$ onto a chosen basis set of fixed localized functions, as we discussed extensively in Refs. [10–12]. There, we have shown that the real space Hamiltonians $\hat{H}(\mathbf{r}_\alpha)$ can be directly calculated using atomic orbitals or PAOs from the pseudopotential of any given element. The key in this procedure is in the mapping of the *ab initio* electronic structure (solved on a well-converged and large plane-waves basis set) into a model that precisely reproduces a selected number of bands of interest [10,11].

The crucial quantities that measure the accuracy of the basis set are the projectabilities $p_{n\mathbf{k}} = \langle\psi_{n\mathbf{k}}|\hat{P}|\psi_{n\mathbf{k}}\rangle \geqslant 0$ ($\hat{P}$ is the operator that projects onto the space of the PAO basis set, as defined in Ref. [11]), which indicate the representability of a Bloch state $|\psi_{n\mathbf{k}}\rangle$ on the chosen PAO set. Maximum projectability, $p_{n\mathbf{k}} = 1$, indicates that the particular Bloch state can be perfectly represented in the chosen PAO set; contrarily, $p_{n\mathbf{k}} \approx 0$ indicates that the PAO set is insufficient and should be augmented. Once the Bloch states with good projectabilities have been identified, the TB Hamiltonian is constructed as:

$$\hat{H}(\mathbf{k}) = AEA^\dagger + \kappa(I - A(A^\dagger A)^{-1}A^\dagger), \tag{1}$$

where E is the diagonal matrix of KS eigenenergies and A is the matrix of coefficients obtained from projecting the Bloch wavefunctions onto the PAO set (see Ref. [11]). Since the filtering procedure introduces a null space, the parameter κ is used to shift all the unphysical solutions outside a given energy range of interest.

The procedure provides an accurate real space representation of the *ab initio* Hamiltonian $\hat{H}(\mathbf{r}_\alpha)$ as a TB matrix of very small dimension, a crucial advantage for the accurate calculation of any physical properties that requires the precise integration in the reciprocal space.

By exploiting the PAO projection scheme described above we can easily Fourier transform the TB real space representation, interpolate to arbitrary precision, and perform derivatives in reciprocal space. For example, the expectation value of the momentum operator, which is the main quantity in the definition of both and transport and optical descriptors described below, is computed as:

$$\begin{aligned}\mathbf{p}_{nm}(\mathbf{k}) &= \langle\psi_n(\mathbf{k})|\hat{p}|\psi_m(\mathbf{k})\rangle \\ &= \langle u_n(\mathbf{k})|\frac{m_0}{\hbar}\vec{\nabla}_{\mathbf{k}}\hat{H}(\mathbf{k})|u_m(\mathbf{k})\rangle\end{aligned} \tag{2}$$

with

$$\vec{\nabla}_{\mathbf{k}}\hat{H}(\mathbf{k}) = \sum_\alpha i\mathbf{r}_\alpha \exp(i\mathbf{k}\cdot\mathbf{r}_\alpha)\hat{H}(\mathbf{r}_\alpha), \tag{3}$$

$\hat{H}(\mathbf{r}_\alpha)$ being the real space TB matrix and $|\psi_n(\mathbf{k})\rangle = \exp(-i\mathbf{k}\cdot\mathbf{r})|u_n(\mathbf{k})\rangle$ the Bloch's functions.

B. Boltzmann transport

Within the semiclassical theory, the electrical conductivity can be evaluated by solving the Boltzmann equation that describes the evolution of the distribution function f of an electron gas under external electric field and in presence of scattering mechanisms [19–21]. In the so-called scattering-time approximation, the conductivity tensor σ_{ij} can be expressed as an integral over the Brillouin zone (BZ):

$$\sigma_{ij} = \frac{e^2}{4\pi^3}\int_{BZ}\tau\sum_n v_n^i(\mathbf{k})v_n^j(\mathbf{k})\left(-\frac{\partial f_0}{\partial\epsilon}\right)d\mathbf{k}, \tag{4}$$

where τ is the constant relaxation time, $v_n^i(\mathbf{k})$ is the ith component of the electron velocity ($\mathbf{v}_n$) corresponding to the nth band for each $\mathbf{k}$ point in the BZ, f_0 is the equilibrium distribution function, and ϵ is the electron energy.

Generalizing Eq. (4) it is also possible to define analog expressions for the Seebeck-coefficient S and the electron contribution to thermal conductivity κ_{el}. Following the notation of

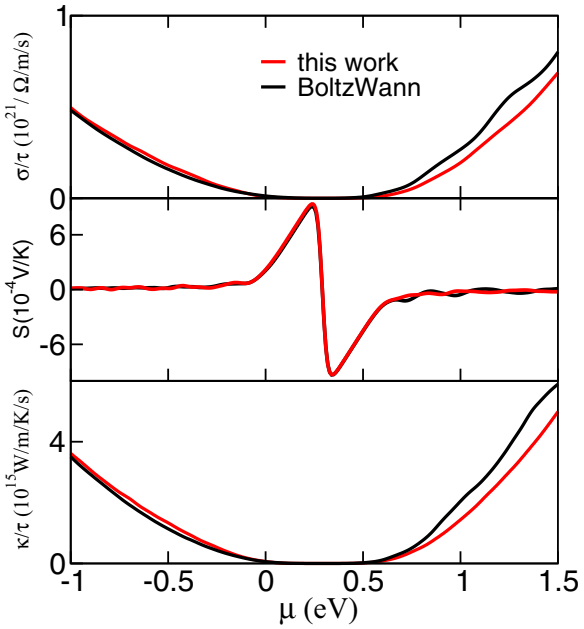

FIG. 1. Boltzmann conductivity, Seebeck coefficient, and electron thermal conductivity for silicon calculated with BOLTZWANN and with our approach, both within the constant relaxation time approximation.

Ref. [22], we introduce the generating tensors $\mathcal{L}_\alpha$ ($\alpha = 0,1,2$):

$$\mathcal{L}_\alpha = \frac{1}{4\pi^3}\int \tau \sum_n \mathbf{v}_n(\mathbf{k})\mathbf{v}_n(\mathbf{k})\left(-\frac{\partial f_0}{\partial \epsilon}\right)[\epsilon_n - \mu]^\alpha d\mathbf{k}, \quad (5)$$

where $\mathbf{v}_n(\mathbf{k})\mathbf{v}_n(\mathbf{k})$ indicates the dyadic product and μ is the chemical potential. The coefficients σ, S, and κ_{el} can be expressed as follows:

$$\begin{aligned} \sigma &= e^2\mathcal{L}_0 \quad S = -\frac{1}{Te}[\mathcal{L}_0]^{-1}\cdot\mathcal{L}_1 \\ \kappa_{el} &= \frac{1}{T}(\mathcal{L}_2 - \mathcal{L}_1\cdot[\mathcal{L}_0]^{-1}\cdot\mathcal{L}_1), \end{aligned} \quad (6)$$

where T is the temperature. From Eqs. (4)–(5) it is evident that the evaluation of the transport properties requires an accurate integration over a fine grid of k point in the BZ, especially for highly dispersive bands as in metal systems. This becomes a trivial task using the TB representation from the PAO projections and Eq. (3). As a validation of this approach we have calculated the transport coefficients (σ, S, κ_{el}) of Silicon and compared with the results of the code BOLTZWANN, where the interpolation of the real space Hamiltonian is done in using maximally localized Wannier functions as basis functions [17]. The results are summarized in Fig. 1 and show excellent agreement between the two approaches.

C. Ballistic transport

Calculations of the ballistic electrical conductance in the manner of Landauer are naturally built on a local representation of the electronic structure such as the one provided by TB Hamiltonians. Our procedure reduces the problem of calculating electron transport [16,23] to a computationally inexpensive postprocessing maintaining the predictive power and the accuracy of first-principles methods. Briefly, using the Landauer approach the conductance is determined via the transmission function that can be written as [23,24]:

$$\mathcal{T}_{el} = \mathrm{Tr}\left(\Gamma_L G_C^r \Gamma_R G_C^a\right),$$

where $G_C^{\{r,a\}}$ are the retarded and advanced Green's functions of the conductor, respectively, and $\Gamma_{\{L,R\}}$ are functions that describe the coupling of the conductor to the leads. The Green's function for the whole system can be explicitly written as [25]:

$$G_C = (\epsilon - H_C - \Sigma_L - \Sigma_R)^{-1}, \quad (7)$$

where Σ_L and Σ_R are the self-energy terms due to the semi-infinite leads.

Once the self-energy functions are known, the coupling functions $\Gamma_{\{L,R\}}$ can be easily obtained as [25]

$$\Gamma_{\{L,R\}} = \mathrm{i}\left[\Sigma^r_{\{L,R\}} - \Sigma^a_{\{L,R\}}\right].$$

The expression of the self-energies can be deduced along the lines of Ref. [23] using the formalism of principal layers in the framework of the surface Green's function matching theory. We obtain:

$$\begin{aligned} \Sigma_L &= H_{LC}^\dagger\left(\epsilon - H_{00}^L - \left(H_{01}^L\right)^\dagger \overline{T}_L\right)^{-1} H_{LC} \\ \Sigma_R &= H_{CR}\left(\epsilon - H_{00}^R - H_{01}^R T_R\right)^{-1} H_{CR}^\dagger, \end{aligned} \quad (8)$$

where $H_{nm}^{L,R}$ are the matrix elements of the Hamiltonian between the layer orbitals of the left and right leads respectively, and $T_{L,R}$ and $\overline{T}_{L,R}$ are the appropriate transfer matrices. The latter are easily computed from the Hamiltonian matrix elements via an iterative procedure [23]. This approach has been extensively validated and it is standard procedure in many electronic structure software packages such as WANT [16], WANNIER90 [15], and SMEAGOL [26].

Acting as postprocessing of static electronic structure calculations, the present implementation is not self-consistent in the bias, as in the nonequilibrium Green's function (NEGF) framework. However, current-voltage characteristics can be actually obtained very reliably in the linear response regime for low applied bias ($\leqslant$1.0 eV) [25]. In most cases, this is accurate enough to reproduce the experimental results, as demonstrated, for instance, in the case of molecular junctions [27], nanotubes [28], and thin nanowires [29]. Moreover, inelastic scattering contributions (e.g., el-el, el-ph) can be easily included as self-energy contributions to the conductor Green's function, along the line proposed by Meir and Wingreen [30] and successfully demonstrated for el-el correlation in the present framework [31].

D. Dielectric function

The optical properties of a material are generally described in semiclassical linear response theory by the dielectric tensor $\epsilon(\omega,\mathbf{q})$ that is a complex function describing the optical response of the material in the presence of an external electromagnetic field at a given frequency ω and momentum $\mathbf{q}$ [19,32]. Quantities such as the refraction index and the absorption spectrum are easily derived from the real and imaginary part of the dielectric tensor. In the limit of long wavelength (i.e., negligible momentum transfer $\mathbf{q}$), the optical

properties of the material depends only on the frequency of the field. The dielectric tensor can then be expressed in terms of the dielectric susceptibility $\chi_{ij}(\omega)$:

$$\epsilon_{ij}(\omega) = 1 + 4\pi\,\chi_{ij}(\omega). \tag{9}$$

Following the seminal work by Graf and Vogl [33], the imaginary part of $\chi(\omega)$ in the single-particle approximation can be written as:

$$\mathrm{Im}\,\chi_{ij}(\omega) = \frac{e^2\pi}{\omega^2\hbar m_0^2\Omega}\sum_{n,m,\mathbf{k}}[f_n(\mathbf{k}) - f_m(\mathbf{k})] \times p^i_{nm}(\mathbf{k})p^j_{mn}(\mathbf{k})\delta[\omega - \omega_{mn}(\mathbf{k})], \tag{10}$$

where m_0 is the bare electron mass, Ω the unit cell volume, m,n the band indices, $f_\ell(\mathbf{k})$ the Fermi-Dirac distribution evaluated on the band with index ℓ at energy $E_\ell(\mathbf{k})$, $p^i_{nm}(\mathbf{k})$ are the matrix elements of the momentum operator calculated over the states (both occupied and empty) with indices m and n and $\hbar\omega_{mn} = E_m(\mathbf{k}) - E_n(\mathbf{k})$ is the energy of the optical transition. The real part of the dielectric susceptibility can then be expressed as the Kramers-Kronig transformation of the imaginary part

$$\mathrm{Re}\,\chi(\omega) = \frac{2}{\pi}\int_0^\infty z\frac{\mathrm{Im}\,\chi(\omega)}{z-\omega}dz. \tag{11}$$

Equation (10) implicitly contains both intraband ($n = m$) and interband ($n \neq m$) transitions. Interband transitions are associated to the usual optical absorption processes in the UV-visible range, while intraband transitions are relevant in the low-frequency regime. In the latter case, Eq. (10) naturally discriminates the different trends of quasistatic dielectric function [$\epsilon(\omega \to 0)$] for insulating (finite behavior) and metallic (diverging behavior) systems. In order to separate the intraband and interband contributions, we rewrite the expression $[f_n(\mathbf{k}) - f_m(\mathbf{k})]$ that appears in Eq. (10). The presence of δ function selects the energy of the transitions $E_n(\mathbf{k}+\mathbf{q}) = E_n(\mathbf{k}) + \hbar\omega$ and, consequently, it fixes the argument of the Fermi-Dirac distributions. Thus for $n = m$ we obtain:

$$f_n(\mathbf{k}) - f_n(\mathbf{k}+\mathbf{q}) = f[E_n(\mathbf{k})] - f[E_n(\mathbf{k}) + \hbar\omega] \approx -\hbar\omega\frac{\partial f(E)}{\partial E}|_{E=E_n(\mathbf{k})}. \tag{12}$$

In the case of undoped semiconductors and insulators the intraband transitions do not contribute to Eq. (10), the imaginary part of the dielectric function vanishes, while the real part tends to static dielectric constant in the collisionless limit. For metallic systems the presence of partially occupied bands at the Fermi energy makes the derivative in Eq. (12) converging to a finite quantity, while the term $\frac{1}{\omega^2}$ in Eq. (10) diverges. The divergency of the dielectric function gives rise to the well-known Drude-like dc conductivity of metals, where electrons close to Fermi-level can undergo electron transitions with negligible momentum transfer in the quasistatic regime ($\omega \to 0$).

The evaluation of the momentum matrix elements, $p^i_{nm}(\mathbf{k})$, is a computational bottleneck since it requires an integration over all the pairs of occupied and empty electronic states across the whole BZ. If the single-particle wave functions are expanded in large basis sets (e.g., plane waves), as in standard solid-state implementations, this integration rapidly becomes a computational challenge. Once again, the momentum can be efficiently evaluated using the TB Hamiltonian projected on the PAOs, transforming the calculation of the frequency-dependent dielectric function into a computationally trivial postprocessing of the first-principles calculation.

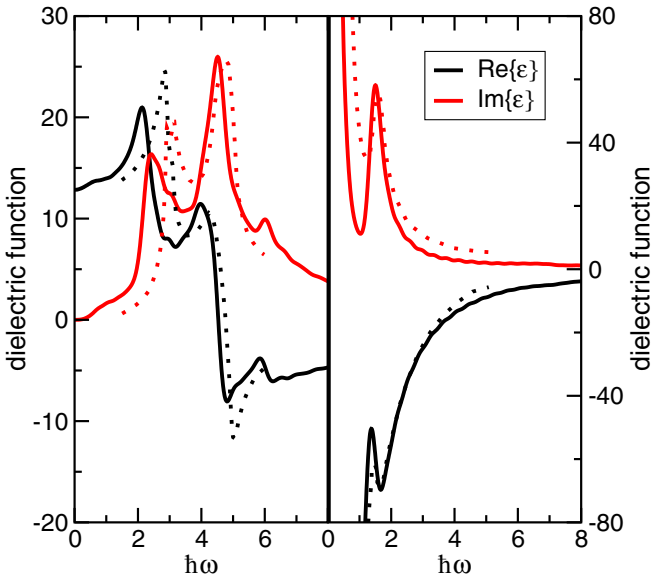

FIG. 2. Real and imaginary part of the dielectric function for GaAs (left) and Al (right). Results are validated against experimental data: Ref. [34] for Al and Ref. [35] for GaAs.

We have validated the method for calculating the dielectric function against well-known experimental results for GaAs and Al. Results are summarized in Fig. 2 and the comparison confirms the validity of our approach.

E. ACBN0 functional

The knowledge of first-principles-based localized orbital representation of the electronic structure combined with analytical expressions based on Gaussian basis set provides an efficient strategy for the fast computation of two-electron integrals for solid-state applications and the development of local exchange functionals (LEX). This is a critical advantage when dealing with the plethora of novel materials that are characterized by strong electron localization and correlation and vigorously sought for their rich physical and chemical properties. For these materials the LDA+U method, introduced by Liechtenstein and Anisimov [36,37], is the most practical choice to compensate for the simplified, nearly homogeneous electron-gas treatment of the electron density by LDA. The success of LDA(GGA)+U confirms that preserving the information of orbital localization from being averaged out is prevalent to the correct prediction of the electronic structure in compounds such as transition-metal oxides [38].

Our projection methodology allows the direct computation of two-electron integrals and, when combined with a density-matrix-based approach, the direct and self-consistent evaluation of the on-site Coulomb U and exchange J parameters needed in the treatment of correlated solid materials. This is at the core of the definition of the ACBN0 functional, recently

introduced by some of us [18]. ACBN0 satisfies the rather ambitious criteria outlined by Pickett *et al.* [39] in one of the seminal articles on LDA+U. Due to the projection on AOs and the accurate TB representation, the evaluation of the U and J for atoms in different chemical environments or close to topological defects (surfaces, interfaces, impurities, etc.) or for closed-shell atoms (like Zn) becomes trivial, thus overcoming the limitations of traditional linear response techniques [40]. Results so far are striking: comparisons with available experimental and theoretical data show that the proposed computation of the on-site Coulomb and exchange parameters is a sound and high-throughput alternative to higher levels of theory such as hybrid functionals and the GW approach that systematically yields results with outstanding accuracy [18,41]. ACBN0 only demands computational resources comparable to a regular (LDA) PBE calculation.

III. COMPUTATIONAL DETAILS

Ground-state properties are obtained with density functional theory as implemented in the QUANTUM ESPRESSO package [42]. The starting electronic structure has been determined using ACBN0 and compared, when appropriate, with traditional PBE. Ionic potentials are described by pseudopotentials with an extended basis set of pseudoatomic orbitals for an improved TB mapping of the conduction bands [12]. The workflow to perform all steps of the approach is part of the AFLOWπ software infrastructure [43]. AFLOWπ has been designed for high-throughput first-principles calculations and exploits the projections on PAO and the TB representation for the calculation of the band structure, density of states, transport coefficients, and frequency-dependent dielectric constant. AFLOWπ is integrated with AFLOW [4].

IV. RESULTS

Our TB representation enables studies that involve extremely fine sampling of the full $E_n(\mathbf{k})$ electronic structure and brings within reach nanostructured systems with hundreds of atoms without compromising first-principles accuracy. As examples to validate our methodology we will analyze with unprecedented details the conduction manifold of $CoSb_3$-based thermoelectric materials (Sec. IV A) and a core-shell nanowire with 588 atoms (Sec. IV B).

A. $CoSb_3$

Materials with the skutterudite structure are of great interest for their performance as thermoelectrics (TEs) since they well represent the paradigmatic case of a phonon-glass electron-crystal [20,44–47]. They exhibit low thermal conductivity but also excellent electronic properties and have been studied extensively both theoretically [48,49] and experimentally [50,51]. The thermoelectric performances are characterized by the so-called figure of merit, $ZT = S^2\sigma T/\kappa$, where S is the Seebeck coefficient, σ is the electrical conductivity, κ is the thermal conductivity, and T is the temperature at which the device operates. The prototypical n-type compound within the skutterudites family is $CoSb_3$ [50,52,53]. Indeed, the figure of merit of R-filled $CoSb_3$ with R = Na, Yb, In, Ba, Ce exceeds one in the temperature windows of practical

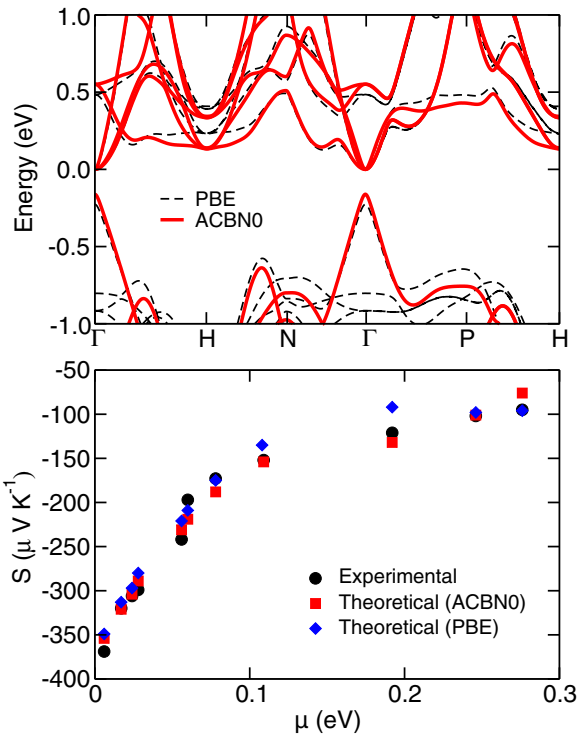

FIG. 3. (Top) Electronic structure of $CoSb_3$. The black-dashed and the red-solid lines refers to PBE [57] and ACBN0 calculations. (Bottom) Seebeck coefficient of $CoSb_3$ measured experimentally (black filled circles) [57] and computed theoretically (red filled squares) with a two-effective-masses model. The energy is measured from the bottom of the conduction band.

interest. Typical descriptors for enhanced TE electronic properties include reasonable large effective masses, which favor large Seebeck coefficients and multivalley character of the active bands to optimize the conductivity [20,54–56]. Doping and filling the semiconducting $CoSb_3$ with donor elements activates the bands at the bottom of the conduction manifold whose features critically contribute to optimize the value of electronic transport coefficients. The enhanced performance of $RCoSb_3$ can be rationalized with a detailed analysis of the full $E_n(\mathbf{k})$ for all the bands in the proximity of the Fermi level. Various experimental and theoretical investigations have been performed in order to highlight the mechanisms responsible for its good thermoelectrical performance and the physics of the system is still under debate. In this paper we extend previous studies on the conduction band of doped $CoSb_3$ (Ref. [57]) by taking advantage the improved band structure provided by the ACBN0 functional discussed in Sec. II E and the Boltzmann transport capabilities presented Sec. II B.

We have computed the starting electronic structure of $CoSb_3$ (prototype: A3B_cI32_204_g_c in Ref. [58]) using a $\mathbf{k}$-point grid of $(9 \times 9 \times 9)$ [57]. The Boltzmann transport coefficients have been then calculated using a much finer grid with $(100 \times 100 \times 100)$ $\mathbf{k}$ points. In Fig. 3(a) we compare the band structure of the system calculated with PBE and ACBN0. Qualitatively, the bands compare well with previous calculations [48], however, in our ACBN0 calculations the energy gap between the occupied and the unoccupied manifold decreases from the PBE value of 0.23–0.16 eV. Both values

are consistent with the experimental findings that range from 0.05–0.22 eV [59], but the reduction of the energy gap may be important to investigate effects associated with decreased performance due to bipolar transport. The linearity of the dispersion [48] at the top of the valence band (p-derived band near Γ) slightly increases and the occupied Co-d manifold moves to lower energy. This is consistent with the fact that the Sb Hubbard correction ($U^{Sb} = 0.648$ eV) is small whereas the value of U for the Co cation ($U^{Co} = 4.375$ eV) leads to a larger variation. This result is of particular importance when chemical substitution is used to reduce the energy separation between dispersive and flat bands in order to optimize the p-type transport coefficients. The description of the conduction manifold also improves. In Fig. 3 (top panel) the valleys at H and along the Γ-N direction in the BZ become quasidegenerate ($\Delta E_{\mathrm{ACBN0}} = 10$ meV) and flatten. It is remarkable that this quasidegeneracy is not captured by standard PBE calculations ($\Delta E_{\mathrm{PBE}} = 100$ meV) [57]. Phenomenologically these effects contribute to increase the number and the effective mass of charge carriers with positive consequences on the conductivity and Seebeck coefficient.

Within the rigid band approximation, we computed the Seebeck coefficient at values of the chemical potential corresponding to the experimental electron density [57] and we compare our theoretical prediction with the experimental results as shown in Fig. 3 (bottom panel). In order to obtain the value of μ corresponding to a given experimental electron density n_e, we have used the free-electron 3D gas relationship $\mu = \frac{\hbar^2}{2m^*}(3\pi^2 n_e)^{2/3}$ where we have employed two effective masses calculated from the electronic structure at Γ and at H assuming a parabolic dispersion. Results are summarized in Fig. 3(b) where we observe an excellent agreement between the calculated and experimental value of the Seebeck coefficient S.

B. Core-shell nanowire

Quasi-one-dimensional, vertically aligned nanowires can be exploited to construct three-dimensional architectures with demonstrated advantages over conventional planar devices. Nanowires form building blocks for compact ultrafast electronics and optoelectronic devices (e.g., solar cells [60,61], photodetectors [62], nanoscale lasers [63], and light-emitting diodes [64,65]). One-dimensional (1D) component-modulated materials, such as coaxial core-shell heterojunctions offer the benefit of designing and fabricating nanodevices without further assembling and provide unique and tunable properties [66–68].

To highlight the capability of our methodology in evaluating the optical and transport properties of nanoscale systems, we have chosen as a prototypical example a coaxial core-shell (CCS) nanowire of ZnO and ZnS [see Fig. 4(b), left inner panel] that has been recently synthesized [69–73].

ZnO has a wide band gap energy of 3.37 eV and it possesses unique optical and electronic properties that make it a promising candidate for UV lasers and detectors working in the 320–400 nm wavelength range. Additionally, it is transparent to visible light and can be made highly conductive by doping [74]. ZnS is also a wide band gap semiconductor, with band gap energy of 3.66 eV widely exploited for optoelectronic devices and sensors. The electrical and the optical characterization of ZnS coated ZnO nanowires have been studied extensively both experimentally [75–80] and theoretically, although on much smaller diameter wires [81].

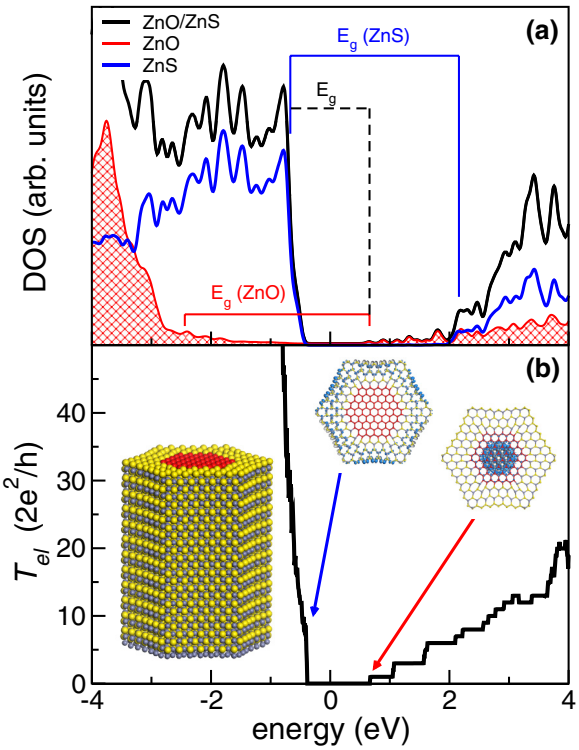

FIG. 4. (a) Total and material-projected density of states plot; (b) quantum conductance. Left inner panel: geometry of the CCS nanowire. Right inner panels: eigenchannels of the transmission amplitude corresponding to the top of the valence and bottom of conduction bands. Zero-energy reference is aligned to the Fermi level of the system.

In this study, the core-shell nanowire is simulated using the ACBN0 functional in a large cell ($50.0 \times 50.0 \times 5.3$) A^3 with 588 atoms (i.e., 5300 electrons). The core is made of ZnO and it has an internal radius $r_c = 1.1$ nm, that is large enough to correctly reproduce a realistic ZnO wire [82]. The shell is made of ZnS, the total radius of the heterostructure is $r_s = 1.9$ nm, in agreement with experimental samples [75]. The wire is aligned along the polar c axis of the wurtzite ZnO crystal. Due to the huge dimension of the system, we include two bilayers of ZnS-ZnO wurtzite material along the wire direction, i.e., the minimum to obtain a periodic wire. The CCS structure has a hexagonal symmetry and exposes only nonpolar $(10\bar{1}0)$ faces. The geometry is fully relaxed until forces on all atoms are lower than 0.03 eV/Å. In the optimized structure the inner ZnO core almost maintains its ideal geometry, while the external ZnS shell undergoes to remarkable distortion due to the relaxation of the mismatch at the interface. Nonetheless the outermost layer exhibits a buckled dimer arrangement, typical of the ZnS$(10\bar{1}0)$ surface (see inset of Fig. 4).

The resulting ACBN0 electronic structure is summarized in Fig. 4(a), where we plot the total (black line), ZnO (red shaded area), and ZnS (blue thin line) projected density of states (DOS). Albeit ZnO and ZnS have similar band gap, the different ionization potential causes the formation of a

staggered type-II band alignment at the interface, with the top of ZnS valence band lying in the pristine gap of ZnO material. The ZnO core has a band gap $E_g \sim 3.1$ eV very similar to corresponding bulk, while the outer ZnS layer has a band gap $E_g \sim 2.8$ eV. This gap reduction derives from the strong atomic deformation, which makes the final structure sensitively different from the ground state bulk one. The total band gap of the CCS nanowire is $E_g \sim 1.2$ eV that lies in the near-IR range.

By using the approach described in Sec. II C, we calculated the coherent electron transport along the nanowire. In the minimal TB representation the solution of the Landauer problem reduces to matrix operations between (2940×2940) on-site and hopping Hamiltonians, i.e., much smaller than the corresponding plane-wave ones. This makes an otherwise unsolvable problem computationally feasible.

For the nanowire we are considering here, the scattering contributions with the boundaries, due to extremely high surface-to-volume ratio, are the predominant effects that control the electron transport [83]. Thus, the coherent regime is a good first approximation for the description of transport, at least at low temperature. The result for the CCS nanowire is shown in Fig. 4(b). The quantum transmittance $\mathcal{T}_{el}$ is proportional to the number of transmitting channels available for electron mobility, which are equal to the number of conducting bands at the same energy. Within the scattering theory framework, the transmittance function $\mathcal{T}_{el}$ can be related to the transmittance amplitude t through the relation $\mathcal{T}_{el} = \mathrm{Tr}[t^{\dagger}t]$. The eigenvectors of matrix t are called eigenchannels and are defined as the linear combinations of the incoming modes in a lead that do not mix upon reflection on the scattering region. Thus, the spatial representation of the eigenchannels visually displays the path traveled by charge carriers in their flow through the nanowire. The eigenchannels corresponding to the top of the valence and bottom of conduction bands are shown as inset in Fig. 4(b): hole carriers flow in the external ZnS crown, while electrons move in the internal ZnO core, confirming the intrinsic charge separation observed experimentally [80].

Simulated optical properties are summarized in Fig. 5. The peaks in the imaginary part of the dielectric function ϵ correspond to single-particle valence-to-conduction transitions. As expected, it is easy to recognize the valence-to-conduction absorption edge in the external ZnS shell (2.8 eV, blue arrow) and in the inner ZnO (3.1 eV, red arrow), which correspond to the E_g values of each material, as discussed above. However, other lower-energy transitions are present in the range 1.2–2.8 eV, which correspond to intermaterial ZnO-to-ZnS transition as depicted in the inset of the figure. Although the frontiers orbitals are mostly localized in the core (electrons) and in the shell (hole), the overlap and the symmetry of the wave functions give low but not negligible oscillator strength to the first four transition. Except for excitonic effects (not included at this level of theory), this agrees well with dramatic

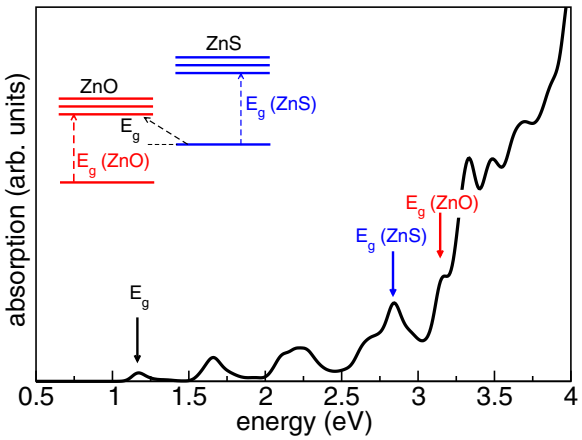

FIG. 5. Imaginary part of dielectric function of ZnS/ZnO CCS nanowire. Inset highlights band-alignment scheme and lowest-energy vertical transitions.

red shift of the absorption edge (i.e., from UV to near-IR) observed experimentally [78,79], also in agreement with previous theoretical calculations on smaller CCS wires [81]. The facile photocharge injection and the intrinsic carrier separation make this system a very promising photoconductor candidate for optoelectronic and photovoltaic devices.

V. CONCLUSIONS

We have extended the PAO projection technique to allow for the calculation of electronic transport and optical properties of materials with extreme accuracy and negligible computational cost. The exact tight-binding representation of the first-principles electronic structure allows, on one hand, to produce extremely dense band interpolations, an essential requirement for the evaluation of Boltzmann transport or optical properties, and on the other, the local Green's function representation that is at the foundation of quantum conductance calculations. We have demonstrated the potentiality of the method by studying the multivalley band structure of $CoSb_3$ and a large ZnO-ZnS core-shell nanowire.

ACKNOWLEDGMENTS

We want to thank the Texas Advanced Computing Center (TACC) at the University of Texas Austin and CINECA for providing computing facilities; the funding provided by DOD-ONR (N00014-13-1-0635, N00014-15-1-2266, and N00014-14-1-0526); the support from the University of Modena and Reggio Emilia through the Grant "Nano- and emerging materials and systems for sustainable technologies"; and the European Union Seventh Framework Program for the Grant Agreement 265073 (ITN-Nanowiring). The authors also acknowledge the Duke University Center for Materials Genomics and the CRAY Corporation for computational assistance.

[1] G. Ceder, D. Morgan, C. Fischer, K. Tibbetts, and S. Curtarolo, Data-mining-driven quantum mechanics for the prediction of structure, MRS Bull. **31**, 981 (2006).

[2] S. Curtarolo, G. L. W. Hart, M. Buongiorno Nardelli, N. Mingo, S. Sanvito, and O. Levy, The high-throughput highway to computational materials design, Nature Mater. **12**, 191 (2013).

[3] S. Curtarolo, W. Setyawan, S. Wang, J. Xue, K. Yang, R. H. Taylor, L. J. Nelson, G. L. Hart, S. Sanvito, M. Buongiorno-Nardelli, N. Mingo, and O. Levy, AFLOWLIB. ORG: A distributed materials properties repository from high-throughput *ab initio* calculations, Comput. Mater. Sci. **58**, 227 (2012).

[4] S. Curtarolo, W. Setyawan, G. L. Hart, M. Jahnatek, R. V. Chepulskii, R. H. Taylor, S. Wang, J. Xue, K. Yang, O. Levy, M. J. Mehl, H. T. Stokes, D. O. Demchenko, and D. Morgan, AFLOW: An automatic framework for high-throughput materials discovery, Comput. Mater. Sci. **58**, 218 (2012).

[5] A. Jain, S. P. Ong, G. Hautier, W. Chen, W. D. Richards, S. Dacek, S. Cholia, D. Gunter, D. Skinner, G. Ceder, and K. A. Persson, The Materials Project: A materials genome approach to accelerating materials innovation, APL Materials **1**, 011002 (2013).

[6] G. Pizzi, A. Cepellotti, R. Sabatini, N. Marzari, and B. Kozinsky, AiiDA: automated interactive infrastructure and database for computational science, Comput. Mater. Sci. **111**, 218 (2016).

[7] E. Hückel, Quantentheoretische Beiträge zum Benzolproblem, Zeitschrift für Physik **70**, 204 (1931).

[8] H. Jones, N. F. Mott, and H. Skinner, A theory of the form of the x-ray emission bands of metals, Phys. Rev. **45**, 379 (1934).

[9] W. Harrison, *Electronic Structure and the Properties of Solids*, 1st ed. (Dover, New York, 1989).

[10] L. A. Agapito, A. Ferretti, A. Calzolari, S. Curtarolo, and M. Buongiorno Nardelli, Effective and accurate representation of extended Bloch states on finite Hilbert spaces, Phys. Rev. B **88**, 165127 (2013).

[11] L. A. Agapito, S. Ismail-Beigi, S. Curtarolo, M. Fornari, and M. Buongiorno Nardelli, Accurate tight-binding Hamiltonian matrices from ab initio calculations: Minimal basis sets, Phys. Rev. B **93**, 035104 (2016).

[12] L. A. Agapito, M. Fornari, D. Ceresoli, A. Ferretti, S. Curtarolo, and M. Buongiorno Nardelli, Accurate tight-binding Hamiltonians for two-dimensional and layered materials, Phys. Rev. B **93**, 125137 (2016).

[13] N. Marzari and D. Vanderbilt, Maximally localized generalized Wannier functions for composite energy bands, Phys. Rev. B **56**, 12847 (1997).

[14] O. K. Andersen and T. Saha-Dasgupta, Muffin-tin orbitals of arbitrary order, Phys. Rev. B **62**, R16219 (2000).

[15] A. A. Mostofi, J. R. Yates, G. Pizzi, Y.-S. Lee, I. Souza, D. Vanderbilt, and N. Marzari, An updated version of wannier90: A tool for obtaining maximally-localised Wannier functions, Comput. Phys. Commun. **185**, 2309 (2014).

[16] A. Calzolari, N. Marzari, I. Souza, and M. Buongiorno Nardelli, Ab initio transport properties of nanostructures from maximally localized Wannier functions, Phys. Rev. B **69**, 035108 (2004).

[17] G. Pizzi, D. Volja, B. Kozinsky, M. Fornari, and N. Marzari, BoltzWann: A code for the evaluation of thermoelectric and electronic transport properties with a maximally-localized Wannier functions basis, Comput. Phys. Commun. **185**, 422 (2014).

[18] L. A. Agapito, S. Curtarolo, and M. Buongiorno Nardelli, Reformulation of DFT+U as a Pseudo-Hybrid Hubbard Density Functional for Accelerated Materials Discovery, Phys. Rev. X **5**, 011006 (2015).

[19] G. Grosso and G. Pastori Parravicini, *Solid State Physics*, 1st ed. (Academic Press, San Diego, CA, 2000).

[20] D. J. Singh, Theoretical and computational approaches for identifying and optimizing novel thermoelectric materials, in *Recent Trends in Thermoelectric Materials Research II*, Semiconductors and Semimetals, edited by T. M. Tritt (Elsevier, Amsterdam, 2001), Vol. 70, pp. 125–177.

[21] G. K. Madsen and D. J. Singh, BoltzTraP. A code for calculating band-structure dependent quantities, Comput. Phys. Commun. **175**, 67 (2006).

[22] N. A. Mecholsky, L. Resca, I. L. Pegg, and M. Fornari, Theory of band warping and its effects on thermoelectronic transport properties, Phys. Rev. B **89**, 155131 (2014).

[23] M. Buongiorno Nardelli, Electronic transport in extended systems: Application to carbon nanotubes, Phys. Rev. B **60**, 7828 (1999).

[24] D. S. Fisher and P. A. Lee, Relation between conductivity and transmission matrix, Phys. Rev. B **23**, 6851 (1981).

[25] S. Datta, *Electronic Transport in Mesoscopic Systems* (Cambridge University Press, Cambridge, 1997).

[26] A. R. Rocha, V. M. García-Suárez, S. Bailey, C. Lambert, J. Ferrer, and S. Sanvito, Spin and molecular electronics in atomically generated orbital landscapes, Phys. Rev. B **73**, 085414 (2006).

[27] X. D. Cui, A. Primak, X. Zarate, J. Tomfohr, O. F. Sankey, A. L. Moore, T. A. Moore, D. Gust, G. Harris, and S. M. Lindsay, Reproducible Measurement of Single-Molecule Conductivity, Science **294**, 571 (2001).

[28] H. T. White and T. N. Todorov, Carbon nanotubes as long ballistic conductors, Nature **393**, 240 (1998).

[29] X. Zhou, S. A. Dayeh, D. Aplin, D. Wang, and E. T. Yuv, Direct observation of ballistic and drift carrier transport regimes in InAs nanowires, Appl. Phys. Lett. **89**, 053113 (2006).

[30] Y. Meir and N. S. Wingreen, Landauer Formula for the Current through an Interacting Electron Region, Phys. Rev. Lett. **68**, 2512 (1992).

[31] A. Ferretti, A. Calzolari, R. D. Felice, F. Manghi, M. J. Caldas, M. Buongiorno Nardelli, and E. Molinari, First-Principles Theory of Correlated Transport through Nanojunctions, Phys. Rev. Lett. **94**, 116802 (2005).

[32] G. Onida, L. Reining, and A. Rubio, Electronic excitations: density-functional versus many-body Green's-function approaches, Rev. Mod. Phys. **74**, 601 (2002).

[33] M. Graf and P. Vogl, Electromagnetic fields and dielectric response in empirical tight-binding theory, Phys. Rev. B **51**, 4940 (1995).

[34] H. Ehrenreich, H. R. Philipp, and B. Segall, Optical properties of aluminum, Phys. Rev. **132**, 1918 (1963).

[35] D. E. Aspnes and A. A. Studna, Dielectric functions and optical parameters of Si, Ge, GaP, GaAs, GaSb, InP, InAs, and InSb from 1.5 to 6.0 eV, Phys. Rev. B **27**, 985 (1983).

[36] V. I. Anisimov, F. Aryasetiawan, and A. I. Lichtenstein, First-principles calculations of the electronic structure and spectra of strongly correlated systems: The LDA+U method, J. Phys.: Cond. Mat. **9**, 767 (1997).

[37] A. I. Liechtenstein, V. I. Anisimov, and J. Zaanen, Density-functional theory and strong interactions: Orbital ordering in Mott-Hubbard insulators, Phys. Rev. B **52**, R5467 (1995).

[38] P. Gopal, R. De Gennaro, M. dos Santos Gusmao, R. Al Rahal Al Orabi, L. Agapito, S. Curtarolo, M. Fornari, and M. Buongiorno Nardelli (unpublished).

[39] W. E. Pickett, S. C. Erwin, and E. C. Ethridge, Reformulation of the LDA+U method for a local-orbital basis, Phys. Rev. B **58**, 1201 (1998).

[40] B. Himmetoglu, A. Floris, S. de Gironcoli, and M. Cococcioni, Hubbard-corrected DFT energy functionals: The LDA+U description of correlated systems, Int. J. Quantum Chem. **114**, 14 (2014).

[41] P. Gopal, M. Fornari, S. Curtarolo, L. A. Agapito, L. S. I. Liyanage, and M. Buongiorno Nardelli, Improved predictions of the physical properties of Zn- and Cd-based wide band-gap semiconductors: A validation of the ACBN0 functional, Phys. Rev. B **91**, 245202 (2015).

[42] P. Giannozzi, S. Baroni, N. Bonini, M. Calandra, R. Car, C. Cavazzoni, D. Ceresoli, G. Chiarotti, M. Cococcioni, I. Dabo, A. Dal Corso, S. De Gironcoli, S. Fabris, G. Fratesi, R. Gebauer, U. Gerstmann, C. Gougoussis, A. Kokalj, M. Lazzeri, L. Martin-Samos, N. Marzari, F. Mauri, R. Mazzarello, S. Paolini, A. Pasquarello, L. Paulatto, C. Sbraccia, S. Scandolo, G. Sclauzero, A. P. Seitsonen, A. Smogunov, P. Umari, and R. M. Wentzcovitch, QUANTUM ESPRESSO: a modular and open-source software project for quantum simulations of materials, J. Phys.: Condens. Matter **21**, 395502 (2009).

[43] A. Supka, T. Lyons, L. Liyanage, D. Ceresoli, R. Al Rahal Al Orabi, P. D'Amico, P. Gopal, A. Calzolari, S. Curtarolo, M. Buongiorno Nardelli, and M. Fornari (unpublished).

[44] G. S. Nolas, J. Sharp, and J. Goldsmid, *Thermoelectrics: Basic Principles and New Materials Developments*, Vol. 45 (Springer, Berlin, 2001).

[45] G. J. Snyder and E. S. Toberer, Morphology control of nanostructures: Na-doped PbTe/PbS system, Nature Mater. **7**, 105 (2008).

[46] J. Sootsman, D. Chung, and M. G. Kanatzidis, New and old concepts in thermoelectric materials, Ang. Chem. Inter. Ed. **48**, 8616 (2009).

[47] G. Chen, M. S. Dresselhaus, G. Dresselhaus, J.-P. Fleurial, and T. Caillat, Recent developments in thermoelectric materials, Int. Mater. Rev. **48**, 45 (2003).

[48] D. J. Singh and W. E. Pickett, Skutterudite antimonides: Quasilinear bands and unusual transport, Phys. Rev. B **50**, 11235 (1994).

[49] D. Wee, B. Kozinsky, N. Marzari, and M. Fornari, Effects of filling in $CoSb_3$: Local structure, band gap, and phonons from first principles, Phys. Rev. B **81**, 045204 (2010).

[50] G. S. Nolas, D. T. Morelli, and T. M. Tritt, SKUTTERUDITES: A phonon-glass-electron crystal approach to advanced thermoelectric energy conversion applications, Annu. Rev. Mater. Sci. **29**, 89 (1999).

[51] C. Uher, Skutterudites: Prospective novel thermoelectrics, in *Recent Trends in Thermoelectric Materials Research I*, Semiconductors and Semimetals, edited by T. M. Tritt (Elsevier, Amsterdam, 2001), Vol. 69, pp. 139–253.

[52] T. Caillat, A. M. Borshchevsky, and J. P. Fleurial, Properties of single crystalline semiconducting $CoSb_3$, J. Appl. Phys. **80**, 4442 (1996).

[53] Y. Tang, S. W. Chen, and G. J. Snyder, Temperature dependent solubility of Yb in $YbCoSb_3$ skutterudite and its effect on preparation, optimization and lifetime of thermoelectrics, J. Materiom. **1**, 75 (2015).

[54] M. Fornari and D. J. Singh, Prediction of room-temperature high-thermoelectric performance in n-type $La(Ru_{1-x}Rh_x)_4Sb_{12}$, Appl. Phys. Lett. **74**, 3666 (1999).

[55] R. Al Rahal Al Orabi, N. A. Mecholsky, J. Hwang, W. Kim, J.-S. Rhyee, D. Wee, and M. Fornari, Band degeneracy, low thermal conductivity, and high thermoelectric figure of merit in SnTe/CaTe alloys, Chem. Mater. **28**, 376 (2016).

[56] P. Sun, B. Wei, J. Zhang, J. M. Tomczak, A. M. Strydom, M. Søndergaard, B. B. Iversen, and F. Steglich, Large Seebeck effect by charge-mobility engineering, Nature Commun. **6**, 7475 (2015).

[57] Y. Tang, Z. M. Gibbs, L. A. Agapito, G. Li, H.-S. Kim, M. Buongiorno Nardelli, S. Curtarolo, and G. J. Snyder, Convergence of multi-valley bands as the electronic origin of high thermoelectric performance in $CoSb_3$ skutterudites, Nature Mater. **14**, 1223 (2015).

[58] M. J. Mehl, D. Hicks, C. Toher, O. Levy, R. M. Hanson, G. Hart, and S. Curtarolo, The AFLOW Library of Crystallographic Prototypes, arXiv:1607.02532 (2016).

[59] Y. Pei, H. Wang, and G. J. Snyder, Band engineering of thermoelectric materials, Adv. Mater. **24**, 6125 (2012).

[60] E. Garnett and P. Yang, Light trapping in silicon nanowire solar cells, Nano Lett. **10**, 1082 (2010).

[61] S. Hu, C.-Y. Chi, K. T. Fountaine, M. Yao, H. A. Atwater, P. D. Dapkus, N. S. Lewis, and C. Zhou, Optical, electrical, and solar energy-conversion properties of gallium arsenide nanowire-array photoanodes, Energy Environ. Sci. **6**, 1879 (2013).

[62] C. Soci, A. Zhang, X.-Y. Bao, H. Kim, Y. Lo, and D. Wang, Nanowire photodetectors, J. Nanosci. Nanotech. **10**, 1430 (2010).

[63] X. Duan, Y. Huang, R. Agarwal, and C. Lieber, Single-nanowire electrically driven lasers, Nature (London) **421**, 241 (2003).

[64] J. Bao, M. A. Zimmler, F. Capasso, X. Wang, and Z. F. Ren, Broadband ZnO single-nanowire light-emitting diode, Nano Lett. **6**, 1719 (2006).

[65] A. T. M. G. Sarwar, B. J. May, J. I. Deitz, T. Grassman, D. W. McComb, and R. C. Myers, Tunnel junction enhanced nanowire ultraviolet light emitting diodes, Appl. Phys. Lett. **107**, 101103 (2015).

[66] L. Lauhon, M. Gudiksen, C. Wang, and C. Lieber, Epitaxial core-shell and core-multishell nanowire heterostructures, Nature (London) **420**, 57 (2002).

[67] J. L. Boland, S. Conesa-Boj, P. Parkinson, G. Tütüncuoglu, F. Matteini, D. Rüffer, A. Casadei, F. Amaduzzi, F. Jabeen, C. L. Davies, H. J. Joyce, L. M. Herz, A. F. i Morral, and M. B. Johnston, Modulation doping of GaAs/AlGaAs core/shell nanowires with effective defect passivation and high electron mobility, Nano Lett. **15**, 1336 (2015).

[68] S. Saha, S. Sarkar, S. Pal, and P. Sarkar, Tuning the energy levels of ZnO/ZnS core/shell nanowires to design an efficient nanowire-based dye-sensitized solar cell, J. Phys. Chem. C **117**, 15890 (2013).

[69] A. Brayek, M. Ghoul, A. Souissi, I. Ben Assaker, H. Lecoq, S. Nowak, S. Chaguetmi, S. Ammar, M. Oueslati, and R. Chtourou, Structural and optical properties of ZnS/ZnO core/shell nanowires grown on ITO glass, Mater. Lett. **129**, 142 (2014).

[70] X. Huang, M. Wang, L. Shao, M.-G. Willinger, C.-S. Lee, and X.-M. Meng, Polarity-Free Epitaxial Growth of Heterostructured ZnO/ZnS Core/Shell Nanobelts, J. Phys. Chem. Lett. **4**, 740 (2013).

[71] W. H. Nam, Y. S. Lim, W.-S. Seo, H. K. Cho, and J. Y. Lee, Control of the shell structure of ZnO–ZnS core-shell structure, J. Nanopart. Res. **13**, 5825 (2011).

[72] X. M. Shuai and W. Z. Shen, A Facile Chemical Conversion Synthesis of ZnO/ZnS Core/Shell Nanorods and Diverse Metal Sulfide Nanotubes, J. Phys. Chem. C **115**, 6415 (2011).

[73] Y. F. Zhu, D. H. Fan, and W. Z. Shen, A general chemical conversion route to synthesize various ZnO-based core/shell structures, J. Phys. Chem. C **112**, 10402 (2008).

[74] Z. L. Wang, Zinc oxide nanostructures: growth, properties and applications, J. Phys.: Condens. Matter **16**, R829 (2004).

[75] J. Li, D. Zhao, X. Meng, Z. Zhang, J. Zhang, D. Shen, Y. Lu, and X. Fan, Enhanced ultraviolet emission from ZnS-coated ZnO nanowires fabricated by self-assembling method, J. Phys. Chem. B **110**, 14685 (2006).

[76] K. Wang, J. J. Chen, Z. M. Zeng, J. Tarr, W. L. Zhou, Y. Zhang, Y. F. Yan, C. S. Jiang, J. Pern, and A. Mascarenhas, Synthesis and photovoltaic effect of vertically aligned ZnO/ZnS core/shell nanowire arrays, Appl. Phys. Lett. **96**, 123105 (2010).

[77] X. Q. Meng, H. Peng, Y. Q. Gai, and J. L, Influence of ZnS and MgO shell on the photoluminescence properties of ZnO core/shell nanowires, J. Phys. Chem. C **114**, 1467 (2010).

[78] X. Fang, Z. Wei, R. Chen, J. Tang, H. Zhao, L. Zhang, D. Zhao, D. Fang, J. Li, F. Fang, X. Chu, and X. Wang, Influence of exciton localization on the emission and ultraviolet photoresponse of ZnO/ZnS core–shell nanowires, ACS Appl. Mater. Interface. **7**, 10331 (2015).

[79] X. Fang, Z. Wei, Y. Yang, R. Chen, Y. Li, J. Tang, D. Fang, H. Jia, D. Wang, J. Fan, X. Ma, B. Yao, and X. Wang, Ultraviolet Electroluminescence from ZnS@ZnO Core–Shell Nanowires/p-GaN Introduced by Exciton Localization, ACS Appl. Mater. Interface. **8**, 1661 (2016).

[80] S. Jeong, M. Choe, J.-W. Kang, M. W. Kim, W. G. Jung, Y.-C. Leem, J. Chun, B.-J. Kim, and S.-J. Park, High-performance photoconductivity and electrical transport of ZnO/ZnS core/shell nanowires for multifunctional nanodevice applications, ACS Appl. Mater. Interface. **6**, 6170 (2014).

[81] J. Schrier, D. O. Demchenko, Lin-Wang, and A. P. Alivisatos, Optical properties of ZnO/ZnS and ZnO/ZnTe heterostructures for photovoltaic applications, Nano Lett. **7**, 2377 (2007).

[82] G. Cicero, A. Ferretti, and A. Catellani, Surface-induced polarity inversion in ZnO nanowires, Phys. Rev. B **80**, 201304 (2009).

[83] A. Catellani, A. Ruini, M. Buongiorno Nardelli, and A. Calzolari, Unconventional co-existence of plasmon and thermoelectric activity in In:ZnO nanowires, RSC Adv. **5**, 44865 (2015).